

Local order in Pt–47 at. % Rh measured with x-ray and neutron scattering

Ch. Steiner,¹ B. Schönfeld,¹ M. J. Portmann,^{1,*} M. Kompatscher,^{1,†} G. Kostorz,¹ A. Mazuelas,² T. Metzger,² J. Kohlbrecher,³ and B. Demé⁴¹ETH Zürich, Institute of Applied Physics, CH-8093 Zürich, Switzerland²ESRF, F-38043 Grenoble, France³Paul Scherrer Institut, CH-5232 Villigen PSI, Switzerland⁴Institut Laue-Langevin, F-38042 Grenoble, France

(Received 21 October 2004; revised manuscript received 15 December 2004; published 25 March 2005)

The diffuse x-ray scattering and small-angle neutron scattering of a Pt–47 at. % Rh single crystal aged at 923 K were measured to determine the local atomic arrangement. The separated short-range order scattering including the small-angle scattering range showed weak intensity modulations, with the maximum at $1\frac{1}{2}0$ positions, thus indicating the presence of local order. In contrast to short-range order scattering, size-effect scattering is already well visible in the raw data, in spite of the small difference of 3% in the atomic sizes. Size-effect scattering is mainly due to Rh-Rh displacements.

DOI: 10.1103/PhysRevB.71.104204

PACS number(s): 61.66.Dk, 64.90.+b

I. INTRODUCTION

Platinum alloys, such as Pt-Rh, are widely used as catalysts, and their microstructure near the surface was repeatedly studied (see Refs. 1 and 2, and references therein). Scanning tunneling microscopy revealed local atomic order and local decomposition in the first layer, depending on the heat treatment after sputtering and the surface orientation.³ Little is known about the microstructure in the bulk. From atom-probe field ion microscopy,⁴ a slight tendency for local decomposition was deduced. Diffuse scattering experiments using x-rays or neutrons have not been performed so far. These methods are very powerful for a quantitative characterization of the local atomic arrangement in the bulk.^{5–9} Since there are a number of conflicting theoretical predictions on the ground state, it was thus indicated to perform such a study.

The phase diagram of Pt-Rh shows complete mutual solid miscibility in the A1 structure at elevated temperatures.¹⁰ A miscibility gap (indicated by a dashed line in Fig. 1) and a critical temperature of 1033 K for Pt–50 at. % Rh (see Fig. 1) are taken from a proposal of Raub.¹¹ This author assumed the presence of decomposition in all binary alloys of fcc Pt metals (Rh, Pd, Ir, Pt) on the basis of the known behavior of Ir-Pt, Ir-Pd, and Pd-Rh and estimated the critical temperature of the miscibility gap by correlating it to the difference of the melting temperatures of the constituents. However, decomposition was later on not found in Pd-Pt by Kidron¹² who used diffuse x-ray scattering.

On the basis of the phase diagrams of binary alloys comprising transition metals (TMs), Bieber and Gautier¹³ suggested Pt-Rh to decompose at low temperature. In general, systems where both constituents are either early or late TMs, should show complete miscibility or decomposition, whereas all other TM systems should show order. Known exceptions are, e.g., Pt base alloys with 3d TMs. These general trends were supported by electronic structure calculations using the generalized perturbation method. As Pt and Rh are both late TMs, decomposition is expected for Pt-Rh alloys.

Based on *ab initio* electronic-structure calculations, Lu *et*

al.^{14,15} proposed several ground state structures for Pt-Rh, all involving $\langle 1\frac{1}{2}0 \rangle$ concentration waves; Pt₄Rh and PtRh₄ with the $D1_a$, PtRh with the “40”, Pt₂Rh₅ with the X2 (Au₅Mn₂), and PtRh₃ with the $D0_{22}$ structure. The order-disorder transition temperatures were below 300 K indicating only weak tendencies for order. At elevated temperatures, a low degree of local order is expected; e.g., for Pt–50 at. % Rh at 600 K, a diffuse maximum with less than 2 Laue units was obtained at $1\frac{1}{2}0$ positions.

In view of these unsettled differences, an experimental determination of the type of order in Pt-Rh may be useful. Small-angle neutron scattering (SANS) experiments and two diffuse x-ray scattering experiments were performed. In all experiments, the same Pt-Rh single crystal was employed. It had been grown with a composition close to 1:1 stoichiometry in order to obtain large diffuse scattering intensities.

(i) A diffuse x-ray scattering experiment was performed with synchrotron radiation to optimize the scattering contrast (the squared difference of the atomic scattering factors of the constituents) by choosing a wavelength close to the Rh-K absorption edge. Thus, the possible presence of local order might be directly visible.

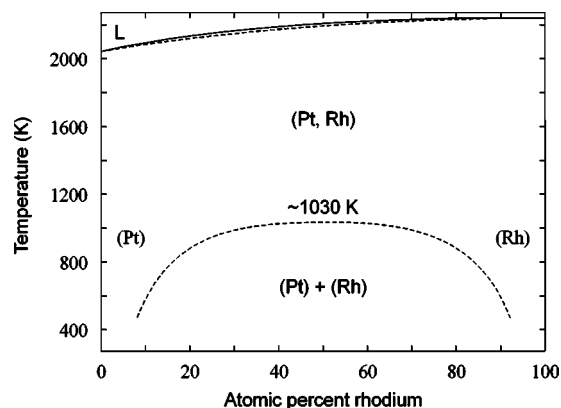


FIG. 1. Phase diagram of Pt-Rh according to Massalski (Ref. 10).

(ii) A detailed diffuse x-ray scattering experiment was done in the laboratory with Mo- K_α radiation to obtain sufficient data for a quantitative analysis of the local atomic arrangements according to the separation techniques of Borie and Sparks¹⁶ and Georgopoulos and Cohen.¹⁷

(iii) The SANS experiments were performed to investigate the possible presence of decomposition. Neutrons are preferred to x-rays in this case as thicker samples can be used.

From the elastic diffuse scattering short-range order and size-effect scattering are determined. Based on these contributions, ground-state structures are discussed employing effective pair interaction parameters obtained by the inverse Monte Carlo method. Also species-dependent static atomic displacements are determined, and a general comparison of published displacement parameters with the type of short-range order is presented.

II. THEORY

The elastic coherent diffuse scattering I_{diff} from crystalline solid solutions is due to the presence of different types of atoms that are not strictly periodically arranged on a lattice and to the static local deviations of the atoms from the sites of the average lattice.^{5,7,18} The scattering contributions are called short-range order scattering I_{SRO} , size effect scattering I_{SE} (linear displacement scattering), and Huang scattering I_{H} (quadratic displacement scattering). The diffuse scattering intensity of a binary A - B alloy is given by

$$I_{\text{diff}}(\mathbf{h})/N = c_A c_B |f_A - f_B|^2 [I_{\text{SRO}}(\mathbf{h}) + I_{\text{SE}}(\mathbf{h}) + I_{\text{H}}(\mathbf{h})] \quad (1)$$

with

$$I_{\text{SRO}}(\mathbf{h}) = \sum_{lmn} \alpha_{lmn} \cos(\pi h_1 l) \cos(\pi h_2 m) \cos(\pi h_3 n), \quad (2)$$

where N is the total number of atoms in the crystal, c_i is the atomic fraction of the component i , f_i its atomic scattering factor, $\mathbf{h}=(h_1, h_2, h_3)$ is the scattering vector in reciprocal lattice units $2\pi/a$ (r.l.u., a =lattice parameter), and the α_{lmn} are the Warren-Cowley short-range order parameters¹⁹ for the lmn type of neighbors (l, m, n in units of $a/2$). The prefactor in Eq. (1), $c_A c_B |f_A - f_B|^2$, is called one Laue unit (L.u.). For a statistically uncorrelated arrangement of atoms on a lattice, all α_{lmn} are zero, except for α_{000} which is unity and short-range order scattering simplifies to the monotonic Laue scattering. Size-effect scattering is given by

$$I_{\text{SE}}(\mathbf{h}) = \sum_i h_i [\eta Q_i^{AA}(\mathbf{h}) + \xi Q_i^{BB}(\mathbf{h})] \quad (3)$$

with, e.g.,

$$Q_x^{AA}(\mathbf{h}) = -2\pi \sum_{lmn} (c_A/c_B + \alpha_{lmn}) \times \langle x_{lmn}^{AA} \rangle \sin(\pi h_1 l) \cos(\pi h_2 m) \cos(\pi h_3 n) \quad (4)$$

and $\eta = \text{Re}\{f_A/(f_A - f_B)\}$, $\xi = \text{Re}\{f_B/(f_A - f_B)\}$. The $\langle x_{lmn}^{\mu\mu} \rangle$ with $\mu=A, B$ are the species-dependent static atomic displacements in units of the lattice parameter a for the lmn type of neighbors.

To separate short-range order scattering from the total diffuse scattering I_{diff} , several techniques have been developed.⁷ While the separation technique of Borie and Sparks¹⁶ is valid only for neutrons, it may also be applied for x-ray data sets if the ratio of the atomic scattering factors of the components A and B , η and ξ , does not vary much with the scattering vector \mathbf{h} . The Borie-Sparks method requires a smaller number of Fourier series for describing displacement scattering, as no species-dependent displacement parameters are determined, but only

$$\gamma_{lmn}^x = -2\pi [\eta (c_A/c_B + \alpha_{lmn}) \langle x_{lmn}^{AA} \rangle - \xi (c_B/c_A + \alpha_{lmn}) \langle x_{lmn}^{BB} \rangle]. \quad (5)$$

The separation technique of Georgopoulos and Cohen¹⁷ can only be applied for x-rays. In the present investigation, both techniques were employed.

III. EXPERIMENT

A single crystal of nominally Pt-50 at. % Rh was grown by electron-beam zone melting, starting with an alloy made of 99.95 at. % pure Pt (Métaux Précieux SA METALOR, Neuchâtel, Switzerland) and 99.98 at. % pure Rh (Johnson Matthey and Brandenberger AG, Zürich, Switzerland). For the x-ray scattering experiments, a disk, 10 mm in diameter and 3 mm in thickness, with a $\langle 421 \rangle$ surface normal, was cut by spark erosion and finally polished with diamond powder of a grain size of $1\mu\text{m}$. The crystal was aged at 1003 K for 26 h, quenched in brine, subsequently aged at 923 K for 36 days, followed by a quench in brine. A stepwise aging was chosen to increase any deviation of a random atomic arrangement in a temperature range where diffusion still prevails. Based on measurements of the electrical resistivity at 77 K of a sample aged between 700 and 1300 K and quenched in brine, it was noted that a state of thermal equilibrium could be set up and frozen in within 24 h between about 900 and 1100 K. For the small-angle neutron scattering experiments, a slice, 0.63 mm in thickness, was prepared from the disk that was used before for diffuse x-ray scattering. All scattering experiments were performed at room temperature. A composition of 47.0(5) at. % Rh was determined by standard-free x-ray fluorescence analysis for the sample disk. Transmission measurements of the thin slice using neutrons at two wavelengths (0.66 and 0.8 nm), yielded a Rh fraction of 46(1) at. %. For the subsequent evaluation, a value of 47(1) at. % Rh was used.

The first diffuse x-ray scattering experiment was done at the ID1 beamline of the ESRF (European Synchrotron Radiation Facility, Grenoble). X-rays with an energy of 23.201 keV (18 eV below the Rh- K absorption edge) were chosen to enhance the scattering contrast $|f_{\text{Pt}} - f_{\text{Rh}}|^2$ by 39% with respect to Mo- K_α radiation. About 4600 positions were measured in a scattering-vector range of 0.8 to 5.0 r.l.u. using a Cyberstar detector with high counting efficiency but an insufficient energy resolution to discriminate the Rh K - $M_{\text{II,III}}$ resonant Raman scattering. The latter was estimated with a Roentec detector that has an energy resolution of about 300 eV, but a low counting efficiency. The background was

20% of the intensity at 0.8 r.l.u. decreasing to about 1% beyond 2 r.l.u. Typically, 4000 to 10 000 counts were registered within 20 s.

For improved counting statistics and more positions, additional measurements were done with a 12 kW Rigaku rotating anode (Mo- K_α radiation) at the laboratory. About 15 800 positions were measured in the scattering-vector range of 1.4 to 7.5 r.l.u. on a grid of 0.1 r.l.u. (with typically 10 000 to 30 000 counts per 220 s, background always <1%). Calibration was done with polystyrene. To correct for surface roughness and the partial passing of the sample by the x-rays at small scattering vectors, the Pt- L fluorescence lines were monitored as a function of the scattering vector.

The static and thermal Debye-Waller factor $\exp[-2(B_{\text{stat}} + B_{\text{dyn}})(\sin \theta/\lambda)^2]$ was calculated on the basis of the elastic constants c_{ij} .²⁰⁻²² These constants were determined by the pulse-echo-overlap method yielding $c_{11}=386(1)$ GPa, $c_{12}=220.6(7)$ GPa, and $c_{44}=136.8(7)$ GPa. Values of $B_{\text{stat}}=0.15 \times 10^{-3} \text{ nm}^2$ and $B_{\text{dyn}}=0.19 \times 10^{-2} \text{ nm}^2$ were obtained. Thermal diffuse scattering up to third order and Compton scattering²³ were calculated and subtracted. Atomic scattering factors and anomalous scattering factors were taken from Refs. 24 and 25.

The SANS experiments were done at SANS-I (SINQ) of the PSI (Paul Scherrer Institut, Villigen) with a neutron wavelength of 0.8 nm ($\Delta\lambda/\lambda=10\%$) and at D11 of the ILL (Institut Laue Langevin, Grenoble) with a neutron wavelength of 0.66 nm ($\Delta\lambda/\lambda=9\%$). Scattering intensities were collected with two-dimensional position-sensitive detectors at distances of 2 or 1.1 m from the sample. Data were corrected for background and converted to scattering cross sections using the elastic incoherent scattering of single-crystalline vanadium. Coherent scattering lengths and absorption and incoherent cross sections were taken from Ref. 26.

IV. RESULTS

A. Small-angle neutron scattering

The SANS intensities of Pt-Rh were always very low, even lower than those of the empty sample holder. As the sample had no high-symmetry orientation and intensities were low, the SANS patterns were azimuthally averaged. The measurements (Fig. 2) did not indicate any intensity increase towards the direct beam. They yielded a nearly constant scattering intensity of 0.2 to 0.5 L.u., well below 1 L.u., the value of the monotonic Laue scattering. Thus, no local decomposition can be inferred from these results.

B. Wide-angle x-ray scattering

Figure 3 (lower triangle) shows the elastic and inelastic scattering in 0.1 L.u. within the (001) plane. The inelastic scattering contributions are seen in the general intensity increase with increasing scattering vectors (Compton scattering) and in the large intensity increase towards the Bragg reflections (thermal diffuse scattering). With respect to the elastic contributions, the large asymmetry in diffuse scattering across the Bragg reflections arises because of size effect

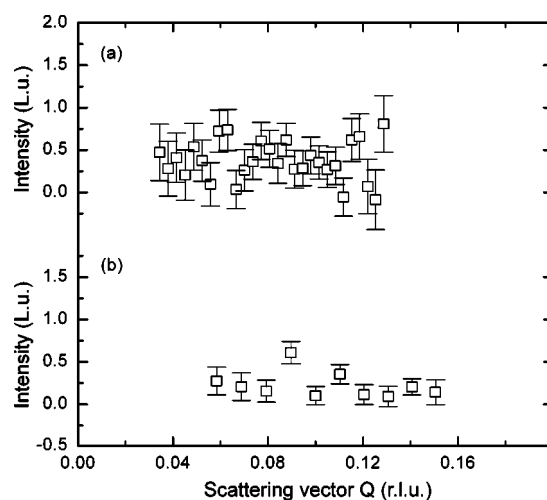


FIG. 2. Small-angle neutron scattering taken (a) with 0.8 nm neutrons at PSI and (b) with 0.66 nm neutrons at ILL.

scattering. There is, however, no obvious maximum between the Bragg positions that would directly reveal the presence of local order. Subsequent measurements at a laboratory x-ray source comprised a four times larger number of \mathbf{h} values. The improved counting statistics and lower background than for the measurement at ID1 allowed an analysis of those scattering data to be performed, and the results are given in the following.

Short-range order scattering was separated employing the Borie-Sparks and the Georgopoulos-Cohen separation techniques. The Warren-Cowley short-range order parameters fitted to the short-range order scattering and the SANS intensities shown in Fig. 2, are given in Table I. The recalculated short-range order scattering is shown in Fig. 4. With 1.5 L.u.,

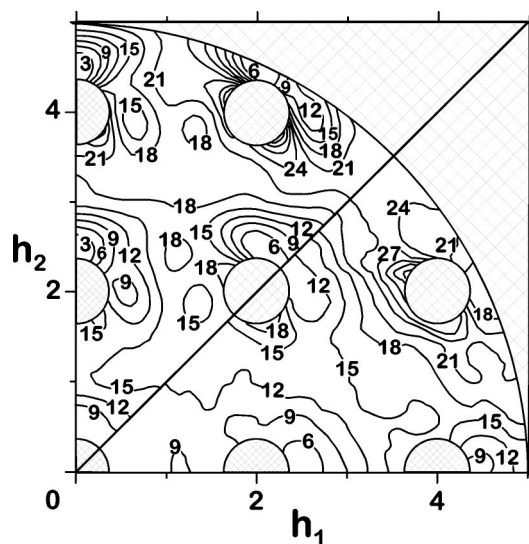


FIG. 3. Elastic and inelastic diffuse x-ray scattering in a (001) plane obtained with x-rays of 23.201 keV energy at ESRF ($h_1 > h_2$). The hatched areas around the Bragg positions indicate the regions of largest thermal diffuse scattering. The isointensity lines are given in 0.1 L.u. For $h_1 < h_2$, the recalculated diffuse scattering is shown using the α_{lmn} and $\langle \chi_{lmn}^{\mu\mu} \rangle$ of Tables I and IV.

TABLE I. Fitted Warren-Cowley short-range order parameters α_{lmn} applying the Borie-Sparks (BS) and the Georgopoulos-Cohen (GC) separation techniques. Also given are the α_{lmn} of the superstructures “40”, X2, $D0_{22}$, and $D1_a$.

lmn	BS	GC	α_{lmn} “40”	X2	$D0_{22}$	$D1_a$
000	1.175(6)	1.102(18)	1	1	1	1
110	-0.046(2)	-0.063(6)	-0.333	-0.283	-0.333	-0.25
200	0.017(2)	0.002(5)	0.333	0.3	0.556	0.167
211	0.001(1)	0.009(2)	0.333	0.183	0.111	0.167
220	-0.007(1)	-0.001(3)	-0.333	-0.167	0.111	-0.25
310	-0.008(1)	-0.015(3)	-0.333	-0.167	-0.333	-0.042
222	-0.009(2)	0.003(4)	-1	-0.4	-0.333	-0.25
321	-0.004(1)		0.333	0.125	0.111	0.167
400	-0.001(2)		1	0.3	1	0.167

the diffuse maximum is low, indicating a low degree of local order in Pt-Rh. This low degree is seen in the magnitude of the nearest-neighbor parameter α_{110} that only amounts to about 6% of its possible maximum value at this concentration. The position of the diffuse maximum at $1\frac{1}{2}0$ coincides with the superstructure position of the suggested structure “40”.¹⁵ As the modulation of the monotonic Laue scattering is small and comparable intensities are also found along [010] where the superstructure reflections of the $D0_{22}$ and $D1_a$ structures (also suggested as superstructures) are located, a discussion of the Warren-Cowley short-range order parameters, an analysis of the nearest-neighbor configurations and a determination of the effective pair interaction parameters is indicated.

V. GROUND STATE STRUCTURES

The fitted Warren-Cowley short-range order parameters of both separation methods generally agree in magnitude and sign, though differences beyond the standard deviations (solely based on counting statistics) are present. The parameter α_{000} lies close to the theoretical value of 1, indicating no

major difficulty in the calibration of the scattering intensities. As less Fourier series are required in the Borie-Sparks evaluation, this separation technique is considered more reliable with the present small modulations. Among the short-range order parameters of the four superstructures of Table I, those of structures “40”, X2, and $D1_a$ agree in sign with the experimental data up to shell 222, only $D0_{22}$ shows less agreement.

To determine characteristic nearest-neighbor configurations (Clapp configurations²⁷), model crystals of $32 \times 32 \times 32$ fcc unit cells with periodic boundary conditions were generated using the α_{lmn} of Table I and those of a random arrangement (with identical composition) in comparison. The ratio in abundances between both states indicates “typical” configurations. For the case of Pt atoms around Rh atoms, the Clapp configurations of the ground state structures suggested by Lu *et al.*¹⁵ are given in Table II (see Fig. 5 for the site occupancies).

In the configurational analysis of a Pt-Rh solid solution, two problems are faced. (i) Only the composition of structure “40” is close to that of the alloy investigated. For the other superstructures, the difference in composition would require a partial replacement with the “wrong” species. (ii) As the degree of short-range order is low, characteristic configurations will not be much enhanced.

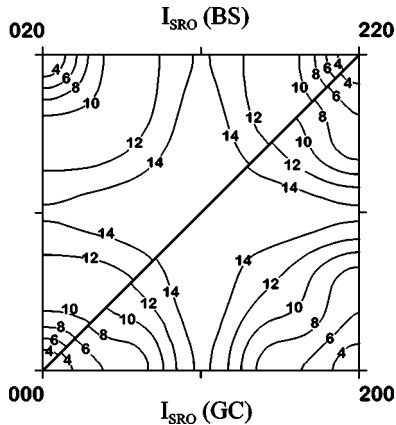


FIG. 4. Recalculated short-range order scattering in 0.1 L.u. using the short-range order parameters of the Borie-Sparks (BS) and the Georgopoulos-Cohen (GC) methods (Table I).

TABLE II. Clapp configurations and site numbering (see Fig. 5) of Pt atoms around a Rh atom for suggested ground state structures.

structure	Clapp configuration	site occupancy
PtRh ₄ ($D1_a$)	C8	5,6,12
PtRh ₃ ($D0_{22}$)	C16	5,6,7,8
	C17	4,6,7,9
Pt ₂ Rh ₅ (X2)	C16	5,6,7,8
	C17	4,6,7,9
	C38	3,5,6,9,11
PtRh (“40”)	C128	1–3,5,8,10–12
Pt ₄ Rh ($D1_a$)	C144	1–12

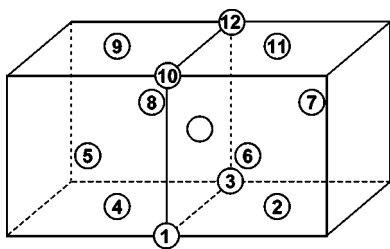


FIG. 5. Coordination polyhedron of the nearest neighbors with site numbering.

Configuration C128 (with the case of Pt atoms around Rh atoms) is found to be most enhanced with an enhancement factor of 2.2 and an abundance of 0.1%. Enhancement factors of other Clapp configurations are ≤ 2 and abundances are typically a few tenths of a percent. The element of the “40” structure is also found to be most enhanced when considering the other three cases (Rh around Rh, Pt around Pt, and Rh around Pt). Considering the other suggested superstructures, none of those is enhanced in its building elements independent of the choice of the central atoms, especially not Pt_2Rh_5 (X2) being closest in composition. It is concluded that a configurational analysis only supports the suggested structure “40”.

Alloys with diffuse maxima at $1\frac{1}{2}0$ positions are well known (see, e.g., Hata *et al.*²⁸ for a discussion of the underlying microstructure), but were not yet reported for solid solutions close to 1:1 stoichiometry. Thus, Pt-Rh seems to be an excellent candidate for the structure “40” that is rarely found (according to Wolverton and Zunger,²⁹ it is not known for any alloy, only for the compounds NbP and TaP).

Effective pair interaction parameters V_{lmn} were determined by the inverse Monte Carlo method³⁰ from the set of α_{lmn} values in Table I. For a canonical ensemble and a binary A - B alloy they are introduced by the Hamiltonian H

$$H/N = c_A c_B \sum_{lmn} V_{lmn} \alpha_{lmn} \quad (6)$$

with $V_{lmn} = \frac{1}{2}(V_{lmn}^{AA} + V_{lmn}^{BB}) - V_{lmn}^{AB}$. The modeled short-range ordered crystals consisted of $32 \times 32 \times 32$ atoms with linear boundary conditions. About 820 000 virtual exchanges were considered. To find the relevant set of effective pair interaction parameters, their number was varied and the V_{lmn} ob-

TABLE III. Effective pair interaction parameters V_{lmn} as obtained by the inverse Monte Carlo method with the α_{lmn} of Table I.

lmn	V_{lmn} (meV)	
	BS	GC
110	8.0(4)	11.7(17)
200	-1.4(3)	1.3(12)
211	0.4(2)	-1.4(5)
220	1.3(4)	-0.2(3)
310	0.9(2)	
222	0.9(3)	

tained were then used in Monte Carlo simulations to determine Warren-Cowley short-range order parameters and to compare them with the experimental parameters of Table I. The values and standard deviations of V_{lmn} are summarized in Table III.

The values of the effective pair interaction parameters V_{lmn} are low. Values of similar magnitude were obtained for, e.g., Ag-Au where the short-range order scattering also shows highest intensities across 110 positions along $\langle 100 \rangle$, but with additional intensity maxima at 100 positions.³¹ As relaxation times for ordering are not known for Pt-Rh, but expected to be large,³² the V_{lmn} parameters might be slightly larger than those given in Table III.

The order-disorder transition temperature T_d was determined by Monte Carlo simulations employing crystals of $16 \times 16 \times 16$ fcc unit cells and periodic boundary conditions. The starting crystal was stoichiometric with structure “40”. Using the V_{lmn} of Table III, a value of 185(15) K was obtained for T_d . This low value compares favorably with the range of transition temperatures (of 90 to 210 K in Ref. 31) obtained for the transition temperatures of the $L1_2$ and $L1_0$ superstructures in Ag-Au.

VI. STATIC ATOMIC DISPLACEMENTS

Sets of displacement parameters (Table IV) were fitted to the separated size-effect scattering as obtained by the Borie-Sparks and the Georgopoulos-Cohen methods. Size-effect scattering recalculated with the fitted parameters of the Borie-Sparks method is shown in Fig. 6 and compared with the contribution to the size-effect scattering solely based on

TABLE IV. Static atomic displacements $\langle x_{lmn}^{\text{RhRh}} \rangle$ and $\langle x_{lmn}^{\text{PtPt}} \rangle$ and the displacement parameters γ_{lmn}^x in units of the lattice parameter a from the Borie-Sparks (BS) evaluation and from the Georgopoulos-Cohen (GC) method with averaged values of η and ξ .

lmn	$\langle x_{lmn}^{\text{RhRh}} \rangle$	$\langle x_{lmn}^{\text{PtPt}} \rangle$	γ_{lmn}^x (BS)	γ_{lmn}^x (GC)
110	-0.0075(6)	0.0006(2)	-0.0413(9)	-0.0418
200	-0.0193(19)	-0.0079(7)	0.0114(31)	0.0094
211	-0.0007(6)	0.0002(2)	-0.0057(10)	-0.0061
121	0.0008(3)	0.0006(1)	-0.0037(16)	-0.0039
220	-0.0043(8)	0.0019(3)	-0.0039(14)	-0.0036

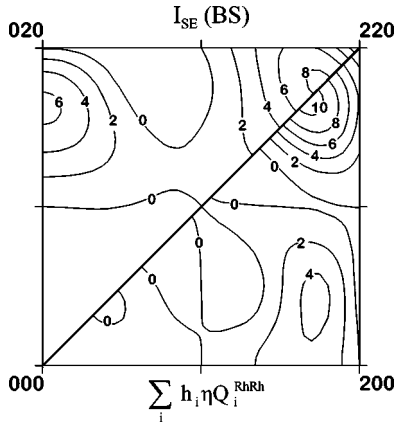


FIG. 6. Recalculated size-effect scattering in 0.1 L.u. using the displacement parameters of the Borie-Sparks (BS) method and the contribution solely based on Rh-Rh displacements (Table IV).

Rh-Rh displacements $\sum_i h_i \eta Q_i^{\text{RhRh}}(\mathbf{h})$. One notices that the major intensity modulation visible as the strong asymmetry across the Bragg reflections in Fig. 3, is due to Rh-Rh displacements. The values of $\gamma_{lmn}^x(\text{BS})$ closely agree with $\gamma_{lmn}^x(\text{GC})$ determined with $\eta=1.897$ and $\xi=0.897$ (values are averages within the range of scattering vectors employed) (Table IV). If one recalculates the elastic (with the atomic displacements $\langle x_{lmn}^{\mu\nu} \rangle$ of Table IV) and inelastic diffuse scattering for the x-ray measurement at ID1, a general agreement is observed (Fig. 3, upper triangle); differences in intensity typically amount to 0.3 L.u., the difference between the equidistant lines. The main feature, the asymmetry in scattering across the Bragg reflections, is reproduced, though in a slightly more pronounced way. The Huang scattering missing in the recalculated diffuse scattering does not show up as a large contribution. Note that the data taken at ID1 were first calibrated with polystyrene, but still had to be scaled by a factor of 1.37. This scaling factor was determined as the ratio between the diffuse scattering within 0.25 r.l.u. around the Bragg reflections (dominated by thermal diffuse scattering) and the calculated inelastic and elastic scattering based on the results of the home laboratory measurement (Tables I and IV). This factor also equals the ratio of the Warren-Cowley short-range order parameter α_{000} of the (unscaled) diffuse wide-angle scattering experiment and the α_{000} of Table I.

Species-dependent atomic displacements were calculated within the theory of Froyen and Herring³³ as the underlying assumptions of a random arrangement and similar atomic sizes are valid for Pt-Rh. Using the elastic constants of the present investigation and the lattice parameter change with composition $a^{-1}da/dc=0.028$ of Ref. 32, the species-dependent nearest-neighbor displacements $\langle x_{110}^{\text{PtPt}} \rangle=0.0026$ and $\langle x_{110}^{\text{RhRh}} \rangle=-0.0029$ are obtained. They are of similar magnitude and have the same signs as the experimental data of Table IV.

On the basis of an Hamiltonian that comprises (i) an Ising term with pair interaction parameters that depend on the displacements, (ii) the elastic energy, and (iii) a term for the coupling between displacements and site occupancy, Chakraborty³⁴ used simple inequalities between the static

atomic displacements for nearest neighbors (NN) of an *A-B* alloy and correlated them with the type of short-range order; $\langle x_{\text{NN}}^{AB} \rangle < (\langle x_{\text{NN}}^{AA} \rangle + \langle x_{\text{NN}}^{BB} \rangle)/2$ for an alloy with local order and $\langle x_{\text{NN}}^{AB} \rangle > (\langle x_{\text{NN}}^{AA} \rangle + \langle x_{\text{NN}}^{BB} \rangle)/2$ for an alloy with local decomposition [in a hard sphere model, $\langle x_{\text{NN}}^{AB} \rangle = (\langle x_{\text{NN}}^{AA} \rangle + \langle x_{\text{NN}}^{BB} \rangle)/2$]. If the $\langle x_{110}^{\mu\nu} \rangle$ of Table IV are employed, local decomposition is expected for Pt-47 at. % Rh, in conflict with the sign of α_{110} .

The correlations between short-range order and the static displacements had been implemented in Ref. 34 on the basis of two experiments and two effective-medium-theory calculations. In the following, a more comprehensive set of published data is checked for these suggested correlations. Experimentally, species-dependent static atomic displacements may be obtained from diffuse scattering by the Georgopoulos-Cohen and the 3λ methods (see Refs. 7 and 8, and references therein). The advantage of the 3λ method (only possible for alloys with elements nearby in the periodic table) is the experimental separation of any scattering contribution that does not depend on the scattering contrast. Both methods do not impose any restriction on the values of $\langle x_{lmn}^{\mu\nu} \rangle$ except that the weighted average displacements of the species-dependent atomic displacements must be zero for any shell *lmn*. With respect to the 3λ method, the correlations are always fulfilled; for local order in Ni-Fe (Ref. 35) and Ni-Cr (Ref. 36) and for local decomposition in Fe-Cr (Ref. 37). Within the Georgopoulos-Cohen analysis, the correlations are fulfilled for local order in Ni-Al (Ref. 38) and for local decomposition in Al-Zn (Ref. 39) and Fe-Cr (Ref. 7). However, for the majority of species-dependent atomic displacements obtained by the Georgopoulos-Cohen analysis, the correlations are not fulfilled; neither for local order in Cu-Au (Ref. 40) and Ni-Cr (Ref. 36), nor for local decomposition in Al-Cu (Refs. 41 and 42) and Cu-Be (Refs. 43 and 44). Certainly, the determination of the species-dependent atomic displacements is delicate, as the evaluation of the same diffuse scattering data with both methods might lead to a fulfillment (Fe-Cr) or nonfulfillment (Ni-Cr) of the correlations. Still, it is expected that most probably the correlations given by Chakraborty³⁴ are too simple to be generally applicable to alloys with any size difference.

VII. CONCLUSION

From the present diffuse scattering pattern of Pt-47 at. % Rh one can conclude that the microstructure is close to that of a statistically uncorrelated alloy. To determine whether local order or local decomposition (as given in current phase diagrams) is present, a combination of small-angle neutron scattering and wide-angle diffuse x-ray scattering was required and the scattering intensities had to be calibrated. The sign sequence of the leading Warren-Cowley short-range order parameters and a configurational analysis of nearest-neighbor configurations support the structure “40” as ground state structure. This superstructure was previously suggested on the basis of *ab initio* electronic-structure calculations for Pt-50 at. % Rh. Species-dependent static atomic

displacements of this alloy as well as of other alloys given in the literature do not support a suggested simple correlation between the type of short-range order and the value of the species-dependent atomic displacements, unless the majority of results obtained by use of the Georgopoulos-Cohen method are discarded.

ACKNOWLEDGMENTS

The authors are grateful to E. Fischer for his support in growing the single crystal. This work was partially supported by the "Schweizerische Nationalfonds zur Förderung der wissenschaftlichen Forschung."

-
- *Present address: Hätschenstr. 12, CH-8953 Dietikon, Switzerland.
 †Present address: PROCEQ SA, CH-8603 Schwerzenbach, Switzerland.
- ¹A. V. Ruban and H. L. Skriver, *Comput. Mater. Sci.* **15**, 119 (1999).
²V. Drchal, A. Pasturel, R. Monnier, J. Kudrnovský, and P. Weinberger, *Comput. Mater. Sci.* **15**, 144 (1999).
³E. L. D. Hebenstreit, W. Hebenstreit, M. Schmid, and P. Varga, *Surf. Sci.* **441**, 441 (1999).
⁴T. T. Tsong, S. B. McLane, Jr., M. Ahmad, and C. S. Wu, *J. Appl. Phys.* **53**, 4180 (1982).
⁵G. Kostorz, in *Physical Metallurgy*, edited by R. W. Cahn and P. Haasen (North-Holland, Amsterdam, 1996), p. 1115.
⁶W. Schweika, *Disordered Alloys: Diffuse Scattering and Monte Carlo Simulations*, Springer Tracts in Modern Physics No. 141 (Springer, Berlin, 1998).
⁷B. Schönfeld, *Prog. Mater. Sci.* **44**, 435 (1999).
⁸G. E. Ice and C. J. Sparks, *Annu. Rev. Mater. Sci.* **29**, 25 (1999).
⁹V. M. Niold and D. A. Keen, *Diffuse Neutron Scattering from Crystalline Materials* (Clarendon, Oxford, 2001).
¹⁰T. B. Massalski, *Binary Alloy Phase Diagrams* (ASM International, Materials Park, Ohio, 1990).
¹¹E. Raub, *J. Less-Common Met.* **1**, 3 (1959).
¹²A. Kidron, *Phys. Lett.* **25A**, 112 (1967).
¹³A. Bieber and F. Gautier, *Acta Metall.* **34**, 2291 (1986).
¹⁴Z. W. Lu, S.-H. Wei, and A. Zunger, *Phys. Rev. Lett.* **66**, 1753 (1991).
¹⁵Z. W. Lu, B. M. Klein, and A. Zunger, *J. Phase Equilib.* **16**, 36 (1995).
¹⁶B. Borie and C. J. Sparks, *Acta Crystallogr., Sect. A: Cryst. Phys., Diffr., Theor. Gen. Crystallogr.* **27**, 198 (1971).
¹⁷P. Georgopoulos and J. B. Cohen, *J. Phys. (Paris), Colloq.* **C7**, 191 (1977).
¹⁸L. H. Schwartz and J. B. Cohen, *Diffraction from Materials* (Springer, Berlin, 1987).
¹⁹J. M. Cowley, *J. Appl. Phys.* **21**, 24 (1950).
²⁰B. E. Warren, *X-ray Diffraction* (Dover, New York, 1990).
²¹S. L. Quimby and P. M. Sutton, *Phys. Rev.* **91**, 1122 (1953).
²²M. A. Krivoglaz, *X-ray and Neutron Diffraction in Nonideal Crystals* (Springer, Berlin, 1996).
²³D. T. Cromer, *J. Chem. Phys.* **50**, 4857 (1969).
²⁴*International Tables for Crystallography*, edited by A. J. C. Wilson (Kluwer, Dordrecht, 1992).
²⁵S. Sasaki (unpublished).
²⁶V. F. Sears, *Neutron News* **3**, 26 (1992).
²⁷P. C. Clapp, *Phys. Rev. B* **4**, 255 (1971).
²⁸S. Hata, S. Matsumara, N. Kuwano, K. Oki, and D. Shindo, *Acta Mater.* **46**, 4955 (1998).
²⁹C. Wolverton and A. Zunger, *Phys. Rev. B* **51**, 6876 (1995).
³⁰V. Gerold and J. Kern, *Acta Metall.* **35**, 393 (1987).
³¹B. Schönfeld, J. Traube, and G. Kostorz, *Phys. Rev. B* **45**, 613 (1992).
³²E. Raub and G. Falkenburg, *Z. Metallkd.* **55**, 392 (1964).
³³S. Froyen and C. Herring, *J. Appl. Phys.* **52**, 7165 (1981).
³⁴B. Chakraborty, *Europhys. Lett.* **30**, 531 (1995).
³⁵X. Jiang, G. E. Ice, C. J. Sparks, L. Robertson, and P. Zschack, *Phys. Rev. B* **54**, 3211 (1996).
³⁶B. Schönfeld, G. E. Ice, C. J. Sparks, H.-G. Haubold, W. Schweika, and L. B. Shaffer, *Phys. Status Solidi B* **183**, 79 (1994).
³⁷L. Reinhard, J. L. Robertson, S. C. Moss, G. E. Ice, P. Zschack, and C. J. Sparks, *Phys. Rev. B* **45**, 2662 (1992).
³⁸P. Georgopoulos and J. B. Cohen, *Acta Metall.* **29**, 1535 (1981).
³⁹D. R. Haeffner and J. B. Cohen, *Acta Metall.* **37**, 2185 (1989).
⁴⁰B. D. Butler and J. B. Cohen, *J. Appl. Phys.* **65**, 2214 (1989).
⁴¹X. Auvray, P. Georgopoulos, and J. B. Cohen, *Acta Metall.* **29**, 1061 (1981).
⁴²E. Matsubara and J. B. Cohen, *Acta Metall.* **31**, 2129 (1983); **33**, 1945 (1985); **33**, 1957 (1985).
⁴³Y. M. Koo, J. B. Cohen, S. M. Shapiro, and L. E. Tanner, *Acta Metall.* **36**, 591 (1988).
⁴⁴Y. M. Koo and J. B. Cohen, *Acta Metall.* **37**, 1295 (1989).